Materials Advances

Accepted Manuscript

This article can be cited before page numbers have been issued, to do this please use: G. Lacarbonara, S. Chini, S. Ratso, I. Kruusenberg and C. Arbizzani, *Mater. Adv.*, 2022, DOI: 10.1039/D2MA00583B.

ROYAL SOCIETY OF CHEMISTRY

rsc.li/materials-advances

MnO_x- graphitic carbon composite from CO_2 for sustainable Li-ion battery anodes.

View Article Online
DOI: 10.1039/D2MA00583B

Giampaolo Lacarbonara[a], Sebastiano Chini[a], Sander Ratso[b], Ivar Kruusenberg[b], Catia Arbizzani[a, *]

[a] *Alma Mater Studiorum - University of Bologna, Dept. of Chemistry "Giacomo Ciamician"*

Via F. Selmi 2, 40126 Bologna, Italy

[b] *National Institute of Chemical Physics and Biophysics,*

Akadeemia tee 23, 12618 Tallinn, Estonia

catia.arbizzani@unibo.it

ABSTRACT

The increasing concentration of CO_2 in the atmosphere is the leading cause of the greenhouse gas effect. Carbon capture and storage is an important topic to develop sustainable technologies. Molten salt CO_2 capture and electrochemical transformation represent a suitable process to produce various carbon products, such as carbon nanofibers, carbon nanotubes, graphite, and graphene. The employment of graphitic anode materials for Li-ion batteries coming from CO_2 capturing is ideal for increasing battery sustainability. Moreover, the addition of transition metal oxides represents a suitable strategy for new negative electrodes because conversion reactions lead to high specific capacities. Among them, manganese has gained attention due to its multiple valence states and numerous possible crystalline structures. In the present work, a MnO_x-graphitic carbon composite obtained by electrolysis of CO_2 via melt Li_2CO_3 is characterized and used to prepare a negative electrode for LIB with an environmentally sustainable aqueous process.

Keywords: CO_2 utilization; MSCC-ET; graphitic anode materials; MnO_x; Li ion batteries

* Corresponding author. Tel: +39 0512099798. E-mail: catia.arbizzani@unibo.it (Catia Arbizzani)

View Article Online
DOI: 10.1039/D2MA00583B

1. INTRODUCTION

EIA estimates that U.S. energy-related CO_2 emissions decreased by 11% in 2020. This decline in emissions was related to economic contraction resulting from the COVID-19 pandemic. In 2021, EIA forecasts energy related CO_2 emissions will increase by about 6% from the 2020 level as economic activity increases and leads to rising energy use [1]. Fossil fuel combustion for energy production is the single largest source of greenhouse gas emissions globally, and CO_2 is also a side product of many key industries such as cement, steel, and aluminum. Reducing CO_2 emissions is one of the most critical challenges of the 21st century. A carbon dioxide sequestration and/or transformation technology is a valuable approach to decrease the CO_2 emission to the atmosphere [2]. Splitting this molecule into C and O_2 transforms a dangerous greenhouse gas into a valuable resource. One proposed method for splitting CO_2 is the molten salt CO_2 capture and electrochemical transformation (MSCC-ET) method [3, 4]. With this method, the CO_2 molecule is transformed into solid carbon and gaseous oxygen via a molten salt intermediate with efficiency typically > 90 % [5]. Various carbon products, such as carbon nanofibers (CNF), carbon nanotubes (CNT), graphite and graphene, have been successfully prepared in molten salts via the MSCC-ET method [6]. Molten Li_2CO_3 has been proven to be the most effective choice of electrolyte media for CNF production, while the addition of Ni or a Ni-based anode has been noted to be crucial for CNF formation during the synthesis [3]. Alternatively, carbonaceous materials can be obtained from the electroreduction of dissolved CO_2 in carbonates [7]. These CO_2 – derived carbons can be utilized by various purposes, including energy storage devices like Li-ion batteries (LIBs).

Currently, mainly two kinds of graphitic material are used in state-of-the-art LIBs – natural graphite and synthetic graphite [3]. The European Union declared natural graphite a critical raw material. On the other hand, synthetic graphite is mainly produced by pyrolysis of unsaturated carbon, which is generally derived from petroleum. Heat treatment includes graphitization at elevate temperatures up to 2500 °C over the longer period, up to several days in some cases [8-11]. Even though the anode material produced this way will lead to higher purity, lower thermal expansion, and overall better battery performance, the relatively high price of the synthetic graphite with respect to the natural graphite is the downside of that material (20 US$ kg^{-1} vs. 8-11 US$ kg^{-1}, respectively [12]. On top of that, synthetic graphite has rather high environmental footprint due to the long treatments at high temperature. However, the greenhouse gases (GHG) emissions are estimated similar to those involved in the refining and purification steps of natural graphite [11].

The possibility to synthesize graphite from sustainable resources would provide the advantage of being independent of natural graphite resources and of expensive and non-environmentally friendly synthetic graphite. The use of graphitic anode materials for Li-ion batteries coming from CO_2

View Article Online
DOI: 10.1039/D2MA00583B

transformation is thereby a solution in line with the EU policy of circular economy, where recycled materials are preferable to the continuous exploitation of new resources.

Besides that, researchers pay significant attention to novel graphitic anode materials, as traditional graphite-anodes show a relatively low charge rate which limits the battery power density [13].

To overcome this drawback, different types of nanomaterials, including nanocarbons such as graphite nanoplatelets, graphene, carbon nanofibers, carbon nanotubes, etc. have been investigated as anodes for LIBs [14, 15].

On top of that, new battery concepts with added transition metal oxides have attracted major attention as anode materials after the first report by Poizot et al. [16]. Metal oxides in the composition of anode materials can lead to the higher theoretical capacity (>700 mAh g^{-1}) than commercial graphite (372 mAh g^{-1}) because of conversion reactions [17, 18]. Among the other transition metal oxides, manganese-based oxides have gained significant attention as the multiple valence states of manganese ions and numerous possible crystalline structures can lead to the higher theoretical capacity of up to 1230 mAh g^{-1} [18]. In addition to that, manganese oxide may exhibit much lower potential than other metal oxides, which are used to gain higher energy density [19]. MnO_2 has been included in CNT and this composite material displayed superior electrochemical performances owing to the pseudocapacitive contribution of MnO_2 in charge storage, as well as high conductivity of N-C layer, and the possibility to adapt the volume changes of MnO during cycling[20]. Other composites materials such as sulfides, selenides, covalent organic frameworks with CNT have demonstrated the significance of carbon incorporation for the advanced anode materials [17, 21-22].

Recently, it has been demonstrated that the CO_2-derived carbon material can be doped *in situ* as it is deposited by additives from the electrolyte mixture and/or electrodes. This can create materials from simply metal-decorated nanoparticles up to carbon/metal oxide composites and composite carbon nanotubes with specific properties [8, 23]. Indeed, the Zn from the galvanized steel cathode used in the synthesis is known to act as a catalyst for graphitization, however, the underlying steel (as in this case) can be rather unstable in the molten carbonate electrolyte, leading to a high metal content in the carbon product [24-26]. Other metals such as Fe are also known to commonly be leached from the electrodes and other metal components of the reactor into the MSCC-ET product in the literature but are either mostly washed out by the HCl treatment or not present in this case [27]. Mn is known to be an effective catalyst for the graphitization of carbon materials at high temperatures (>1400 °C) and can graphitize carbon-containing precursors such as lignin even at temperatures as low as 900 °C [27-29]. The high concentration and mobility of C in the Li_2CO_3 electrolyte can further decrease this temperature, leading to the formation of the graphitic carbon layer on top of the MnO_2.

View Article Online
DOI: 10.1039/D2MA00583B

In the present contribution, the electrolysis of CO_2 via a Li_2CO_3 melt will be used to prepare a composite material of manganese oxides and graphitic carbon. The galvanized steel cathode is used as manganese source on which carbon grow occurs. The resulting material will be fully characterized and used to prepare anode with an environmentally sustainable aqueous process. The electrochemical characterization of the anodes in a conventional organic electrolyte will be presented and discussed.

2 RESULTS AND DISCUSSION

2.1 Carbon synthesis

The carbon is synthesized from CO_2 using the molten salt CO_2 capture and electrochemical transformation (MSCC-ET) method [3, 30] which Ratso et al. has previously used to synthesize CO_2-derived catalyst materials [31-34]. The method is based on capturing CO_2 into molten carbonate salts, where the CO_3^{2-} is in equilibrium with CO_2 in the surrounding atmosphere: $CO_3^{2-} \rightleftarrows CO_2 + O^{2-}$ or $CO_2 + CO_3^{2-} \rightleftarrows C_2O_5^{2-}$. The CO_3^{2-}, in turn, is electrochemically split into carbon and oxygen by a four-electron transfer process: $CO_3^{2-} + 4e^- \rightleftarrows C + 3O^{2-}$ [29, 30]. Oxygen is produced on the other electrode. By using a nickel-chromium anode and a Zn-steel cathode, it is possible to create nucleation sites onto the cathode, where the Ni dissolved in the carbonate salt acts as a growth point for carbon nanofibers and other graphitic carbon structures (reactor scheme in Figure 1).

The average electrical efficiency (i.e. the charge required to deposit the carbonaceous material divided by the charge supplied) for the MSCC-ET syntheses was 86 %. The CO_2 conversion efficiency, evaluated by the ratio between the mass of the deposited carbon and the theoretical mass of carbon that should have been deposited by the amount of electricity that was used during the synthesis was ≈ 100%. Under 900°C in Li_2CO_3, no other products are formed from CO_2 than solid carbon. The amount of CO_2 used for this can be calculated directly from the difference of molar masses, for each molecule of CO_2 one atom of solid carbon will be formed (e.g. for 1 g of carbon ~3.7 g of CO_2 is needed). The mass deposited depends on the current efficiency of the specific experiment as well as the electrode area. For a 5 cm^2 cathode, the common amount of produced corresponds to 0.7-1.3 g. Heating the reactor for the synthesis required 0.6 kWh of energy, but it is to be noted that under sufficient insulation, the process has been shown to be exothermic enough to heat itself [35]. In this case such insulation was neglected out of convenience.

View Article Online
DOI: 10.1039/D2MA00583B

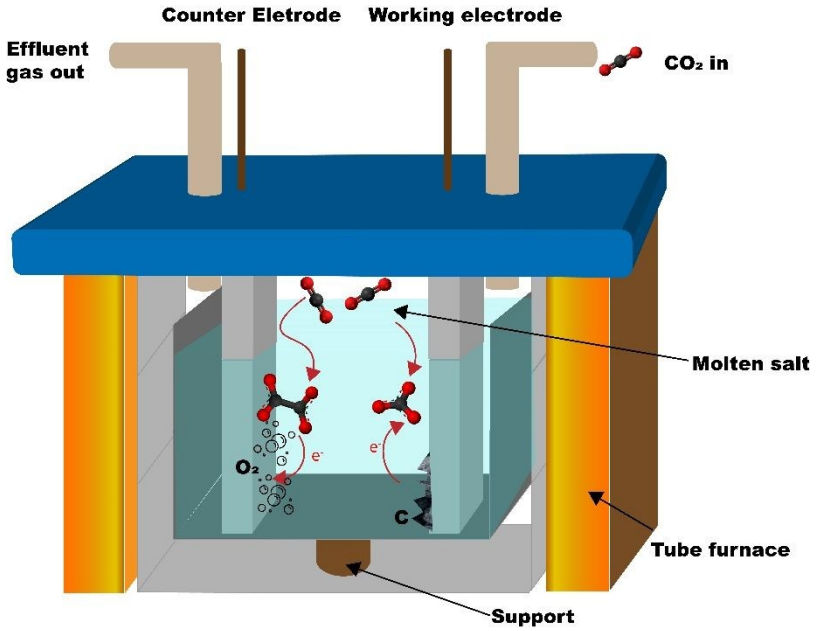

Figure 1. Schematic of the MSCC-ET reactor.

2.2 Physico-chemical characterization of carbons

The scanning electron microscopy (SEM) images of the carbonaceous material is in Figure 2a and the EDS analysis of the selected area is shown in Figure 2b, with the data reported in Table S1 and S2. The synthetized material contains Mn and O, other than carbon arising from the galvanized steel cathode used in the MSCC-ET process. Since the MnO_2 is present even after purification in 5 mol L^{-1} HCl, it is likely that the MnO_2 is protected by a graphitic carbon layer impenetrable by liquid solutions. After milling and sieving with 20 µm sieve (C-20) and 50 µm sieve (C-50), the presence of MnO_x is evidenced by high annular dark field (HADF) scanning transmission electron microscopy (STEM) images, selected area electron diffractograms (SAED), X-Ray diffraction pattern (XRD) and X-ray photoelectron spectroscopy (XPS) spectra, demonstrating the embedding of MnO_x inside the carbon matrix.

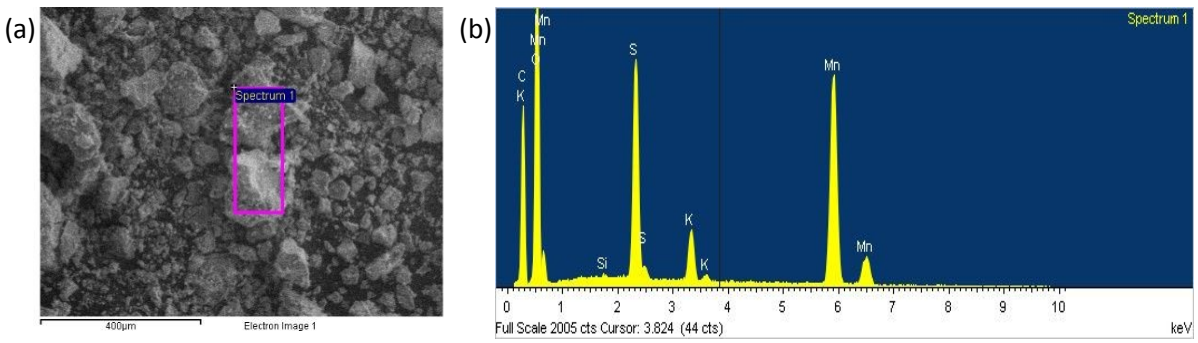

Figure 2. SEM images of (a) pristine carbon ground in agate mortar, (b) EDS analysis of the carbon ground in mortar.

View Article Online
DOI: 10.1039/D2MA00583B

STEM images revealed that MnO_2 is embedded in the carbonaceous matrix (Figure 3a) indeed. Selected area diffraction (SAED) pattern (Figure 3b) reveals the polycrystallinity of MnO_2 with nanocrystals diameter from 10 to 50 nm. The satisfied diffraction condition of the sample's crystal structure observed in the SAED all corresponds with the $Mn_{7.98}O_{16}$.

In the present work, after milling the sample, the MnO_2 is exposed and can contribute to the performance of the cell [36]. Carbon/transition metal oxide composites can have increased power performance and cycling behavior due to pseudocapacitive processes, meaning that the MnO_2 leached from the electrode has a positive effect in this case. However, in the case of undesired phases, further purification of the carbon via treatment in concentrated acids and other oxidizers such prior to HCl washing to expose the metal/metal oxide particles is possible, however, such harsh treatments also modify the structure of the carbon material itself [37].

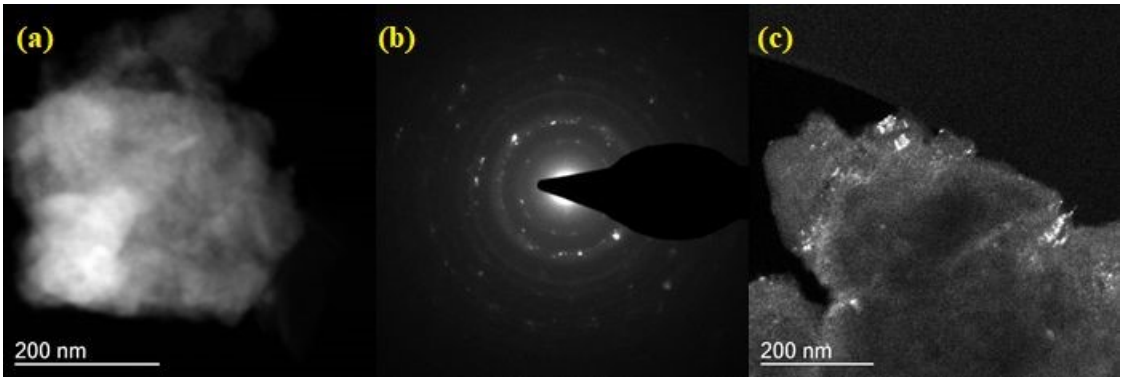

Figure 3. HADF-STEM images of C50 carbon. (b) SAED pattern acquired over an area of 200 nm. (c) HADF-STEM image of C-50 sample selecting the reflection at (d=0.31nm) in the SAED pattern.

The XRD pattern of the pristine synthesized carbon and of C-50 are shown in Figure 4a. In the diffractograms the typical carbon reflections at 26° and 55° are present in addition to several reflections associate to a $Mn_{7.84}O_{16}$ pattern and other metal impurities in the 40°- 45° range. By contrast, the latter are less intense in the pattern of the pristine synthesized carbon before grinding, except that below 20°. This confirms the exposure of MnO_x by milling. X-ray diffraction patterns of manganese oxides materials consist of small signals on a diffuse background due to structural defects. As showed by Julien et al. [36], the particle size and the chemistry of defects lead to the structural differences in the materials. In the material reported, the presence of potassium (Figure 2d) could influence the reflection positioning and intensity.

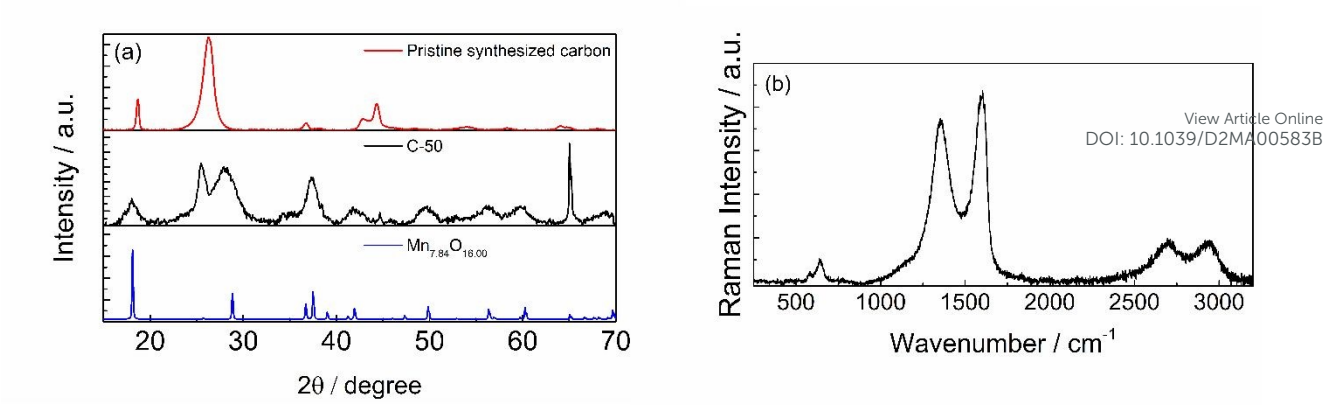

View Article Online
DOI: 10.1039/D2MA00583B

Figure 4. (a) X-ray diffraction pattern of pristine synthesized carbon (red), C-50 (black) and diffractogram of $Mn_{7.84}O_{16}$ (reference code 96-151-4117). (b) Raman spectrum of the carbon ground in agate mortar.

Raman spectra in Figure 4b also confirmed that the synthesized carbonaceous material is graphitic. The characteristic graphite D, G, and 2D bands are present at ca. 1350, 1580, and 2700 cm^{-1}, respectively. Additionally, the Raman spectrum showed reflections that could be attributed to Mn^{2+} at ca. 700 cm^{-1} [37]. The general peculiarity of the vibrational features MnO_2 is their low Raman activity. Generally, the spectrum is characterized by three band at 500–510, 575–585 and 625–650 cm^{-1}. The two high-wavenumber bands have a higher Raman intensity, while low-frequency bands are not visible in the spectrum reported. The two high-frequency band at 640 and 580 cm^{-1} indicate the presence of MnO_2 as romachenite [37].

The full survey XPS spectrum (Figure 5a) of C-50 carbon shows the characteristic peaks of C1s, K2p, O1s, and Mn2p at 284 eV, 292.5 eV, 532 eV, and 641.9 eV, respectively. Atomic percentage quantification is reported in Table 1, weighted composition is obtained by correcting the bands area for the atomic mass. The carbonaceous material shows great presence of carbon and manganese with the oxygen that is involved in manganese oxide phase and oxygen-functional groups in carbon phase. Indeed, the carbon phase contain a 15% of oxygen functionalities in the structure (Table S3).

The XPS high resolution of C1s (Figure 5b) exhibits contributions of C=C carbon at 284.1 eV, C-H at 284.9 eV, C-O-R at 286.0 eV, and C=O at 288.2 eV [38, 39]. These signals overlay with the less intense K2p signals. Also, S2p shows the typical $2p_{3/2}/2p_{1/2}$ doublet separation of 1.18eV with peaks constrained to a 2/1 area ratio ($2p_{3/2}$ / $2p_{1/2}$) (Figure S2) [40].

The O1s region (Figure 5c) present at least three contributions indicating the Mn-O bonds with a prevalence of Mn-O-H terminals (75% from the integrated deconvolution reported in Table S4). This agrees with the presence of a nanocrystalline material with extended boundaries. The Mn2p region (Figure 5d) shows the two signals related to the spin-orbit coupling ($Mn2p_{3/2}$ and $Mn2p_{1/2}$). The

manganese bands result from the contribution of MnO_2 phase at 641.3 eV [41, 42] and Mn_2O_3 at 642.6 eV [41, 42] in a 4:6 ratio (Table S5).

Table 1. Atomic content of C-50 from integrals of C1s, K2p, O1s, S2p, and Mn2p signals.

	Binding energy (eV)	Abundancy (%)	Weighed abundancy (%)
C	1s 284.4	25.9	15.7
K	2p 292.5	1.9	3.2
O	1s 531.5	51.7	35.7
S	2p 168.4	3.2	4.4
Mn	$2p_{3/2}$ 642.2	17.3	41.0

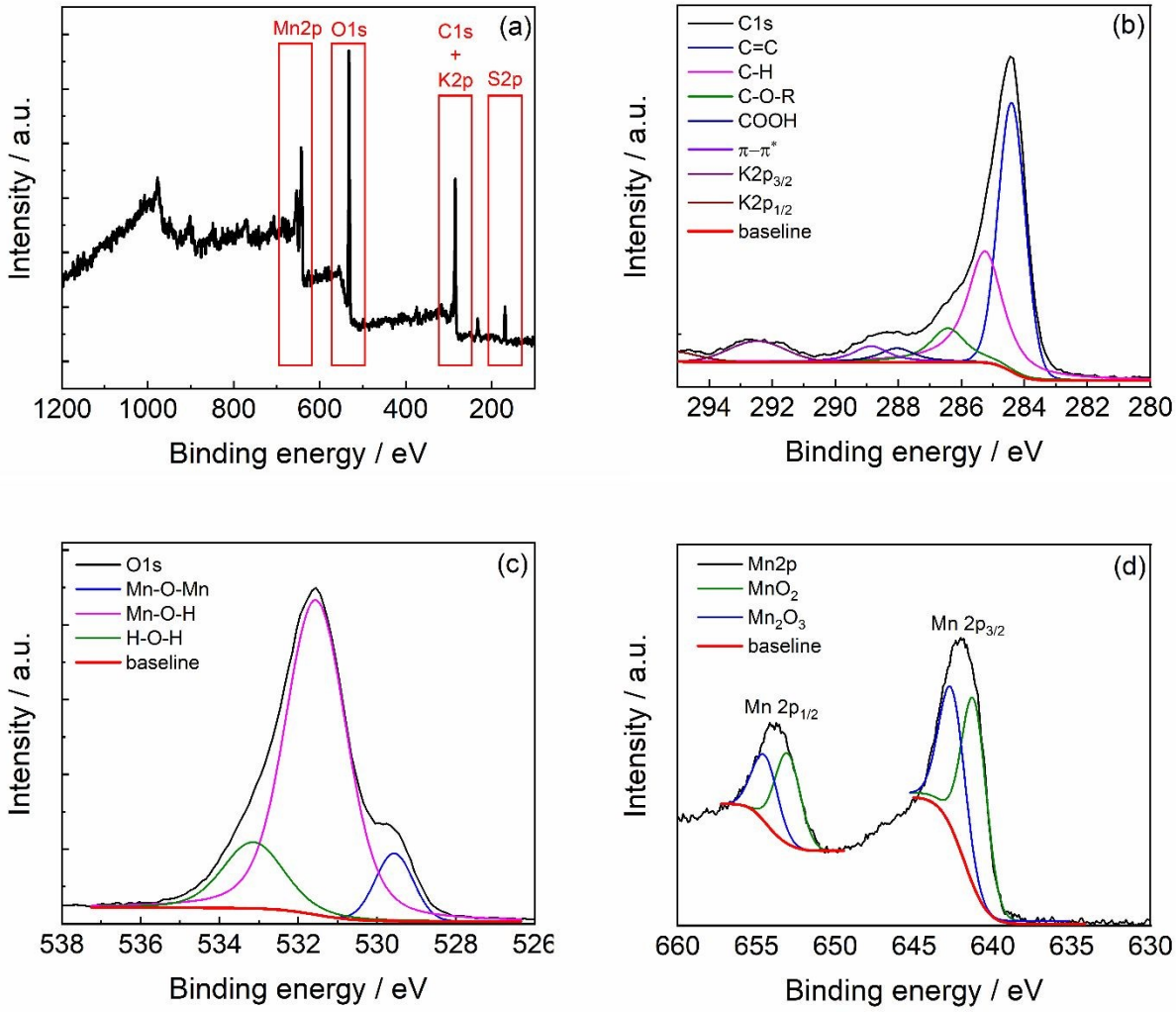

Figure 5. (a) XPS survey spectra of C-50, high-resolution XPS spectra of (b) C1s region, (c) O1s region, and (d) Mn2p region.

View Article Online
DOI: 10.1039/D2MA00583B

Figure 6 shows the TGA analysis in thermal as well as thermo-oxidative conditions. These curves are totally different from pure graphitic materials and evidence the presence of metal oxides. The two curves display almost the same behavior up to 200°C. The sample is stable in Ar up to 500°C, as expected. Hence, above 600°C the mass continues to decrease but at low rate, with a total mass decrease of 45%. This would mean that 55% of C-50 is constituted by inorganic material (presumably oxides), in agreement with SAED and XPS analysis. Hence, the residual quantity, 55% of the total mass, agrees with the MnO_x observed by XPS analysis. The TGA curve in O_2 displays a mass decrease occurring by steps, starting around 250°C, 400°C and 750°C, with a final residue of 45%. This curve is very similar to that of MnO_2 [43], where the mass decreases up to 400°C is explained by the removal of adsorbent, the transformation of MnO_x to the other crystalline oxide phases up to the conversion of MnO_2 to Mn_2O_3 above 700°C with oxygen release. Figure 6b shows the XRD patterns of the residues from the two TGA analyses in Ar and in O_2. The patterns display the presence of MnO in the residue after the TGA in inert atmosphere, and the presence of oxides of Mn(III) and M(IV) formed throughout the TGA in oxygen.

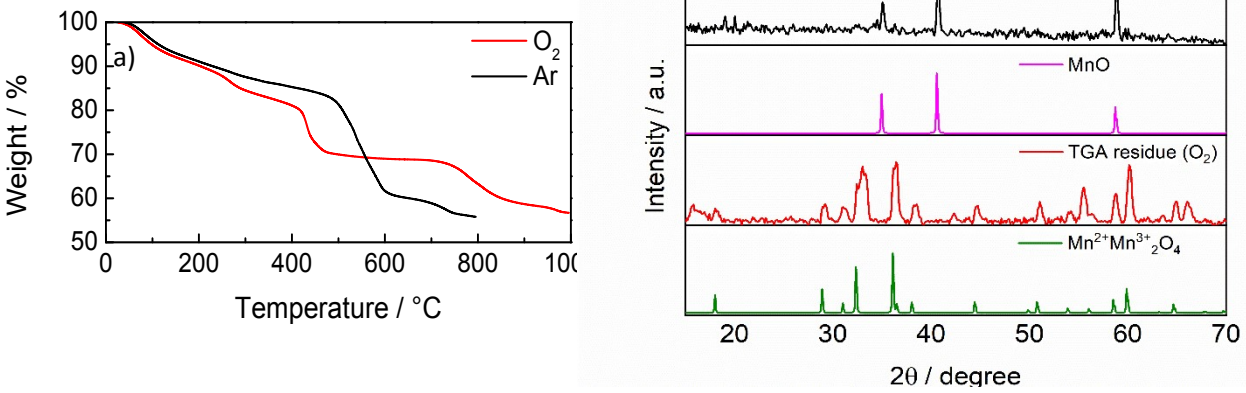

Figure 6. a) TGA curves of C-50 in Ar and in O_2 at 10°C min^{-1}. b) XRD patterns of the residues from the TGA of Figure 6a, of MnO (reference code 01-075-0626) and of Mn_3O_4 (reference code 01-089-4837).

We can estimate that in the reported samples the content of C is less than 50%, by considering that the decrease below 200°C could be also due the adsorbed water and to the oxygen-containing functional groups (15% from XPS analysis) and the remaining ash is mainly constituted of metal oxides.

2.3 Electrochemical characterization of carbons

The high inorganic material content could affect adhesion on Cu current collectors. Indeed, we did not observe any improvement in passing from the coarse C to the more homogeneous C-20 with SA

View Article Online
DOI: 10.1039/D2MA00583B

binder, even by changing the conductive carbon Super C65 with the Super C45, more suitable for aqueous processes. The formation of agglomerate is evident in all the formulation with SA binder and could be justified by the presence of manganese cations that could have a mild and unsteady complexing effect on SA[44]. With the carbon C and C-20 different formulations have been prepared and reported in Table 2.

SEM images of the electrodes with formulation #1 and #4 are in Figure 7. The heterogenicity of the material particles used in electrodes with formulations #1-#3 causes inhomogeneous electrode surfaces that could affect the solid electrolyte interface layer (SEI) formation and cycling. The self-standing electrodes (Figure 7a,b) seems more compact than those from the slurries #2-#3 (Figure 7c-f). Electrode obtained from C-20 (Figure 7g,h) shows increase homogeneous composite with numerous cracks. It's also worth noting that, if the fractures are present only on the electrode surface could positively affect the electrochemical performance, allowing a better wetting of the electrode.

Free-standing electrodes (#1) were too resistive, even the thinnest ones. The electrodes with formulations #2, #3 and #4 gave the voltametric response of the first two cycles is shown in Figure 8.

Table 2. Self-standing and slurries formulation prepared to test the carbonaceous material (indicated as Carbon and abbreviated as C) from MSCCT-ET process.

#	Carbon %	Binder %	Additive %	Dispersing agent	Formulation type	Current collector	Adhesion	mg cm^{-2} active
1	C 90	PTFE 5	Super C65 5	ethanol	solid	none	n.a.	19.8±0.7 3.13±0.06
2	C 80	PVDF 10	Super C65 10	NMP	slurry	Cu	good	3.6±1.2*
3	C 87	SA 3	Super C65 10	water:isopropanol 80:20	slurry	Cu	poor	2.7±0.5
4	C-20 87	SA 3	Super C45 10	water: isopropanol 80:20	slurry	Cu	poor	2.9±1.2*

*The high absolute error is due to the detachment of small portions of the deposit from the current collector. The weight of each electrode was considered for the specific capacity evaluation, not the mean values.

View Article Online
DOI: 10.1039/D2MA00583B

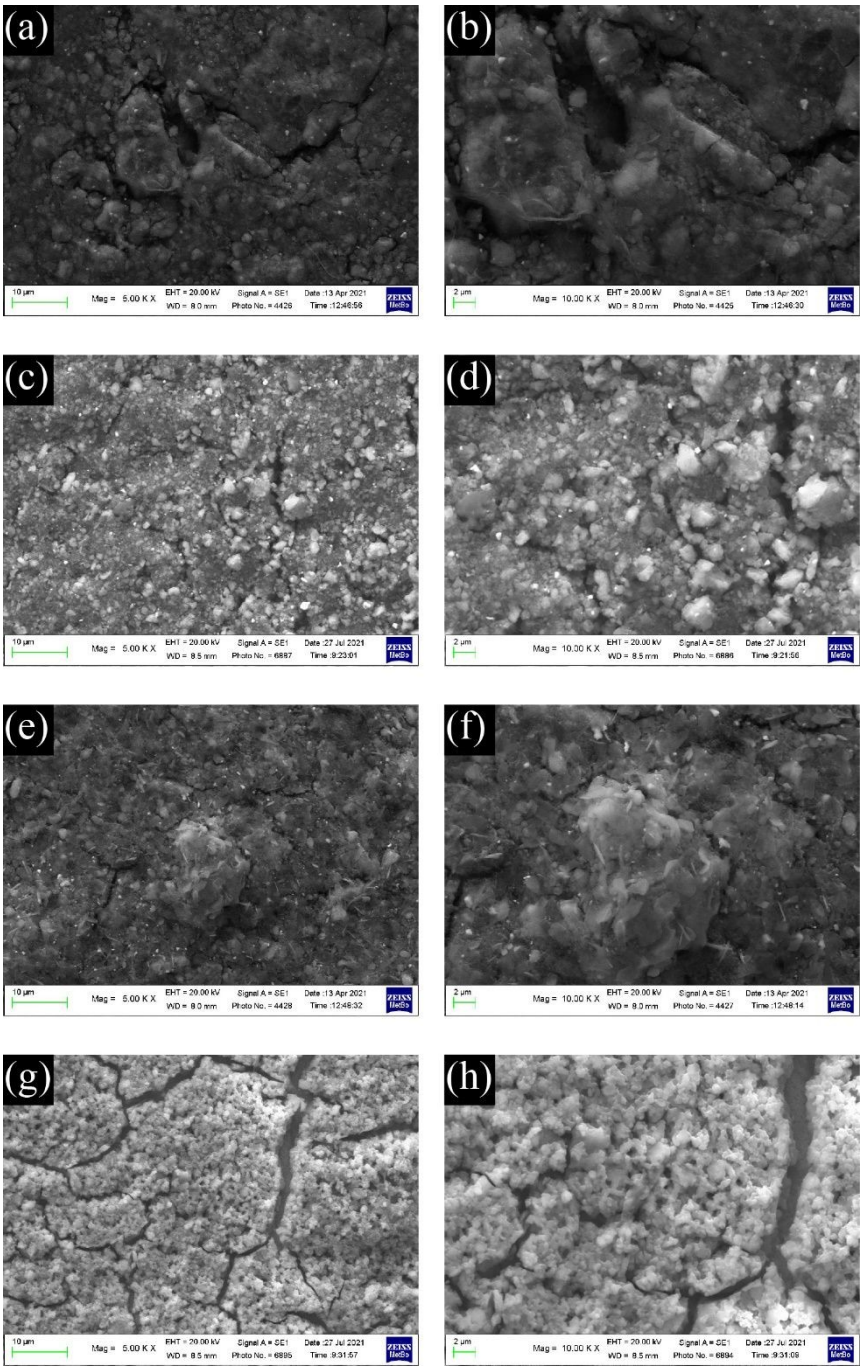

Figure 7. SEM images of electrodes from formulations #1 (a,b), #2 (c,d), #3 (e,f), and #4 (g,h).

As expected, the shape of the CVs is different from that of pure graphite [45]. During the first cycle, in addition to the reduction peak of EC at ca. 0.75 V [46], other reduction processes are present and disappear in the second cycle. The reduction peak is near 0.25 V for both samples, and the oxidation peak is at ca. 1.0 V. These processes are ascribed to the reduction of Mn^{4+} to Mn(0) and to the oxidation of metallic Mn to Mn^{2+}. The further oxidation of Mn^{2+} occurs at potentials higher than 2 V [32]. In the 2nd CV, the reduction broad peak shifts at ca. 0.5 V and remains constant also for the following cycles, indicating the conversion of the Mn_2O_3 and MnO_2 phase (observed in XPS) to MnO.

View Article Online
DOI: 10.1039/D2MA00583B

The reduction of Mn^{4+} and Mn^{3+} to Mn^{2+} occurs during the first reduction process with the formation of Li_2O [36, 47]. In addition, MnO_2 can be lithiated and converted to $LiMnO_2$. In this case, part of the irreversible capacity loss of the first cycle can be attributed to lithium consumption. Also, the conversion reaction of Mn^{2+}/Mn^0 lead to the formation of Li_2O. Li_2O could passivate the electrode, given its not conductive nature, and be responsible for manganese materials' capacity fade [47]. Moreover, the electrode operating potential window was limited to 2V to keep the Mn^{2+} oxidation state, which seems the most promising for the negative electrode in LIBs. Indeed, besides the redox processes occurring between 0 and 2.0 V, the specific capacity of MnO is 756 mAh g^{-1} [47].

The electrode with PVDF binder (#2) displays a lower coulombic efficiency than the electrodes with SA binder (#3 and #4). The higher concentration and more uniform distribution of the carboxylic groups along the SA chains facilitate Li^+ movement and hence, the insertion/deinsertion processes, and can improve the quality of the SEI. For this and other advantageous properties, like the need of lower percentages of binder in the electrode formulation, it was first proposed as a binder for Si-based anode materials [48] and for high voltage cathodes like $LiNi_{0.5}Mn_{1.5}O_4$ [49, 50].

The capacity performance of the formulation #3 with SA was tested in LP30 and in LP30- 2% VC. The rate capability was also compared to that of #2. The current calculated in the rate capability experiments are based on the mass of the active material (carbon and MnO_x).

Figures 9a and 9b report the rate capability and stability tests of formulations #3 (see also Figure S3a). GCD cycles demonstrated that the formulation with PVDF is worse than that with SA, as expected from the low coulombic efficiency evinced from CVs of Figure 8, although the electrode adhesion to current collector is better. The electrode #3 tested in LP30 - 2% VC shows smaller specific capacity at different current regimes. The coulombic efficiency gives scattered values (Figure 9b), indicating that the formed SEI is quite unstable without significantly affecting capacity retention. The addition of VC seems not to improve either the capacity performance or cycle stability. However, the difficulties of obtaining electrodes with a good adhesion may have a role in this evaluation and work in progress to evaluate other current collectors. The stability of #3 electrodes were evaluated after the rate capability test, considering the percentage variation of the electrode theoretical capacity (t. c.) that was obtained from the active material composition from XPS studies (section 2 in Supplementary Information). A 31% graphitic carbon (t. c. 372 $mAhg^{-1}$) contributes to the 20% electrode capacity, while 61% of manganese oxides phase (considered t. c. 756 $mAhg^{-1}$) determines the remaining 80%. Upon cycling (Figure 9b), the electrode capacity approach asymptotically the theoretical capacity of the graphitic phase. Thus, during cycling, the formation of Li_2O lead to an unstable Mn/Mn^{2+} conversion reaction without affecting the insertion/deinsertion process of graphitic carbon. Also,

View Article Online
DOI: 10.1039/D2MA00583B

graphitic carbon seems to exhibit a high capacity approaching the theoretical capacity even if part of the Mn-phase is still electrochemically active.

It has been considered, as the best case for graphite, that the loss of capacity over cycling is mainly due to the MnO_2, also by considering the high loss of the first cycles. It is not possible to assert that graphite remains unaltered over cycling or its specific capacity near the theoretical one. If the graphite has a lower specific capacity, the results indicates that a higher amount of MnO_2 is still working after 200 cycles.

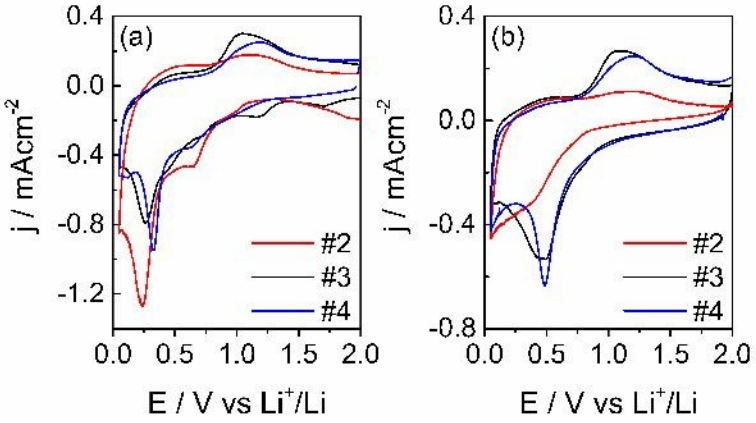

Figure 8. 1st CV (a) and 2nd (b) CV at 50 μV s^{-1} in LP30, WE: carbon electrodes, CE-RE: lithium, separator Whatman: GF/A.

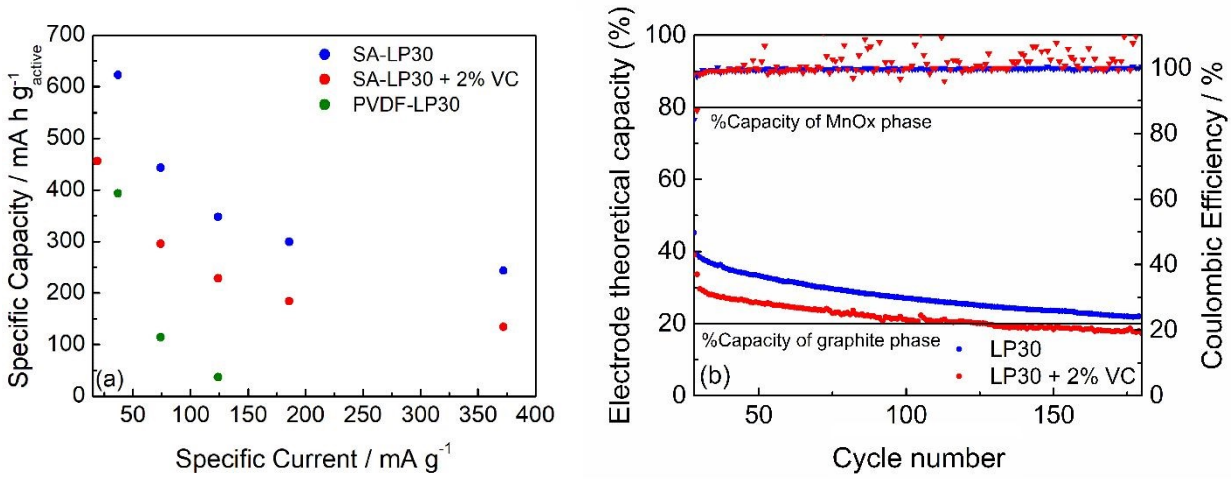

Figure 9. Specific capacity and coulombic efficiency of #3 in LP30 (blue) and LP30 + 2% VC (red) and of #2 in LP30 (green). (a) rate capability test at different specific currents, and (b) stability test at 371 and 186 mA g^{-1} in LP30 and LP30 + 2% VC, respectively.

View Article Online
DOI: 10.1039/D2MA00583B

Limiting the specific current to 100 mA g^{-1}, the GDC cycles demonstrated that the manganese oxides' cycling stability improves with a mild cycling protocol and that the inorganic phase is electrochemically active (Figure 10). The specific capacity is higher if compared to the results reported in Figure 9a at a similar current. This is because the electrode has not performed the initial cycles at very low current rates as in the rate capability test of Figure 9a, where the material stability could have been affected by unwanted and/or irreversible processes, as the low coulombic efficiencies of these cycles testify (Figure S3). The discharge voltage plateau is around 0.5 V, and a not well-defined charge voltage plateau appears around 1.0 V, corresponding to the formation and decomposition of Li_2O and metal nanocrystals with a coulombic efficiency of around 92%. Hence, the repeated volume expansion and contraction of the active particle during cycling affects cycling stability. However, these results indicate that the graphite phase displays a high specific capacity and that the inorganic phase is electrochemically active, even if the stability must be optimized.

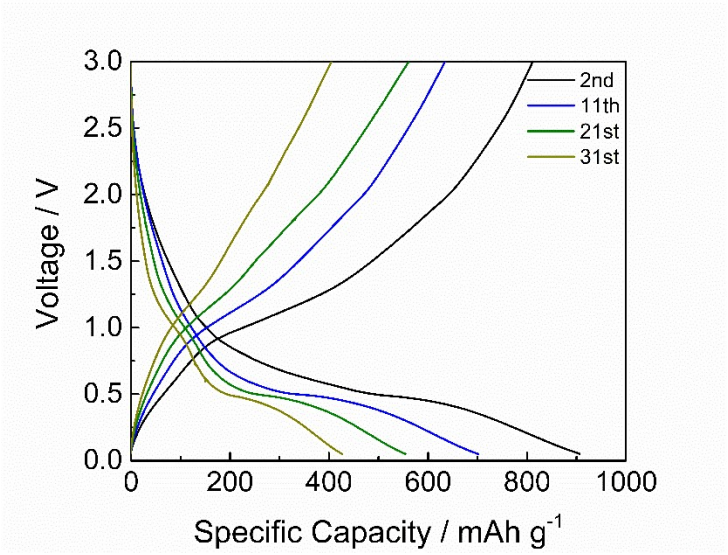

Figure 10. GDC profiles of #3 in LP30 at 100 mA g^{-1}.

This indicates that the graphitic carbon obtained from MSCC-ET is quite promising and the control on the MnO_x content needs to be investigated deeper to exploit the properties of both active materials. Stabilization of MnO_X, reduction of material with H_2 treatment and creation of oxygen vacancies on MnO_2 particles or reducing the amount of MnO_2 with additional acid treatment could be suitable options.

View Article Online
DOI: 10.1039/D2MA00583B

3 CONCLUSIONS

The synthesis of a CO_2-derived battery electrode based on a composite of manganese oxides and graphitic carbon via the MSCC-ET method was demonstrated in this work. The carbon material used for the electrode was synthesized in pure Li_2CO_3 at 770 °C using a NiCr anode and galvanized steel cathode. The latter, lead to a notable concentration (up to 55 wt.%) of manganese oxides into the carbon material as nanocrystals embedded in the carbonaceous matrix as coherently demonstrated by chemical-physical characterizations. The obtained material had been tested as a negative electrode for LIB with an environmentally sustainable aqueous process. In the first cycles, the electrochemical conversion of manganese is demonstrated as the principal faradic process contributing to the electrode capacity. Varying the specific current, the electrode capacity approaches the graphite theoretical capacity asymptotically, demonstrating the good performance of the graphite phase. At the same time, GCD cycles at 100 mA g^{-1} show the feasibility of the manganese oxide phase cycling with high specific capacity. The electrochemical properties of the presented material ought to be optimized, mainly in terms of adhesion to the current collector and granulometry of active material. However, MSCC-ET process, commonly used for carbon allotropes sustainable synthesis, is demonstrated to be a suitable process to obtain nanocrystalline inclusion in a graphitic matrix and pave the way to new methods to produce composite materials. Controlling the amount of MnO_x, its crystalline structure and its distribution in the synthesized carbonaceous material is the goal of this new application for the MSCC-ET process to improve anode performance by taking advantage from the presence of a stable, high-capacity inorganic material like MnO_x.

4 EXPERIMENTAL

4.1. Material synthesis

The carbon is synthesized in an Al_2O_3 crucible (99%, Xiamen Innovacera Advanced Materials Co., China) filled with Li_2CO_3 (p.a., Lachner). The crucible was carefully lowered into a 304 stainless steel reactor tube, as shown in Figure 1. The reactor was then heated to 770 °C and kept at that temperature for an hour to completely melt the Li_2CO_3. A 5 cm^2 NiCr (80% Ni, 20% Cr, Goodfellow, UK) anode and galvanized steel (metall24.ee, Estonia) electrode were then inserted into the carbonate melt. CO_2 was bubbled through the carbonate melt during the electrolysis process at a flow rate of 0.1 SLPM to minimize the formation of lithium oxide, which might get trapped into the material and affect the materials' performance in batteries (Li_2O is generated during the electrolysis process on the cathode along with the carbon with the four-electron transfer reaction shown before and reacts with CO_2 to form lithium carbonate). The oxide tends to be deposited inside of the graphitic carbon structures, making it hard to remove.

View Article Online
DOI: 10.1039/D2MA00583B

The current density was raised with steps of 0.05 A cm^{-2} up to 0.2 A cm^{-2}, with the first two steps taking 5 min and the second two 10 min. This ensures the formation of nickel-based growth nucleation sites on the cathode. After applying 0.2 A cm^{-2} for 10 min the current density was raised to 1 A cm^{-2} and the electrolysis was conducted for 1 h, after which the electrodes were raised out of the carbonate melt. The electrode with the material attached was then cooled down to room temperature and washed with 5 mol L^{-1} HCl (Merck) to remove residual Li_2CO_3 until no bubbling was visible, during which the material detached from the electrode into the acidic solution. The suspension of the material was then vacuum filtered and washed with Milli-Q water until a neutral pH was reached, after which it was dried at 70 °C and weighed.

4.2. Carbon material characterization

The morphology of carbon material and electrodes was investigated by (SEM) by a Zeiss EVO 50 microscope equipped with an energy dispersive X-ray analyzer from Oxford INCA Energy 350 system. STEM images were collected by using a TEM/ STEM FEI TECNAI F20 at 200 keV equipped with an EDS detector in HADF-STEM mode. The powder was dispersed in isopropanol and sonicated for 10 min. TEM gold grid was prepared by drop casting (at 60°C) of the dispersion.

Raman spectroscopy analysis was carried out by a microscope RENISHAW Mod INVIA with an Argon ion Laser (λ=514 nm, 5 scan, 20s, resolution 1-2 cm^{-1}, 50x), while thermogravimetric analysis (TGA) was performed by a TA Instrument Q50 with Ar both as purge and sample gas or with 60 mL min^{-1} Ar as purge gas and 40 mL min^{-1} O_2 as sample gas. XRD patterns were collected on carbon powders by using an x-ray diffractometer PANalytical X'Pert PRO (Malvern Panalytical, United Kingdom) equipped with an X'Celerator detector (Cu K_α radiation, 40 mA, 40 kV).

XPS studies were performed on CF_P samples using a Specs EnviroESCA instrument equipped with an AlKα excitation source (hυ = 1486.7 eV). Survey spectra were collected at an operating pressure of ca. 10-6 mbar in the binding energy (BE) range between 0 and 1460 eV, acquiring data at 100 eV of pass energy, every 1.0 eV·step-1, and at 0.1 sec·step-1. High resolution scans were collected at 40 eV of pass energy, 0.1 eV·step-1, and at 0.5 s·step-1. XPS curves (BE uncertainty = ± 0.2 eV) were fitted by means of the Keystone software provided by Specs and applying a Shirley-type background function [51]. The shift in terms of binding energy was corrected assigning a value of 284.1 / 284.4 eV to the C1s peak attributed to carbon sp2-type [38, 52]. Atomic percentages (at. %) quantification is obtained using the sensitivity factors of integrated peak areas supplied by Specs.

4.3. Electrode preparation

View Article Online
DOI: 10.1039/D2MA00583B

A carbon portion (2 g) was ground in a mortar and then in a planetary mill (Pulverisette 6, Fritsch) with a 14 cm^3 WC jar and 10 WC balls (5 mm diam.) for 15 min at 600 rpm and for 45 min at 450 rpm with the addition of a small amount of water (ca. 2 mL) to improve the grinding (C). Scanning electron microscopy images and electron diffraction spectroscopy analysis are reported in Figure S1 and Table S1). Another portion of carbon (2 g) was ground for 2 hours at 400 rpm in a 70 cm^3 agate jar with 13 agate balls (10 mm diam.) and 4 balls (20 mm diam.). The powder was then sieved with 50 and 20 μm sieves. About 60% of C was collected under the 20 μm sieve (C-20) and 30% under the 50 μm sieve (C-50). The latter portion of material with particle/agglomerate size between 20 μm and 50 μm, was mainly used for physicochemical characterization.

Slurries were prepared by using polyvinilydene difluoride (PVDF, Kynar HSV 900, Arkema) as binder soluble in N-methylpyrrolidone (NMP, Sigma-Aldrich). Slurries and solid composites were prepared with sodium alginate (SA, Sigma Aldrich), Teflon suspension (PTFE, Du Pont aqueous dispersion, Teflon™ 60 wt.%, density 1.5 g cm^{-3}), Na carboxymethyl cellulose (CMC, Sigma Aldrich, ultra-low viscosity) and styrene-butadiene rubber (SBR, Zeon BM 400b) as binder soluble in water. SuperC65 and SuperC65 (Imerys) were used as conducting agents. The formulations were C:PVDF (80:10) for the slurry in NMP, C:SA (87:3), C:CMC:SBR (85:7:3), C:CMC:PTFE (85:7:3) for the slurry in water:isopropanol (80:20) and C:PTFE (90:5) for the free standing electrode. The remaining percentage is carbon additive, as indicated in Table 2. The free-standing electrodes were calendred in order to obtain two different loadings (see Table 2). The slurries were prepared by ball milling carbons in a WC jar with the addition of the binder dissolved in a low amount of water for 90 min at 450 rpm. The slurries were deposited on a Cu foil with a Mini Coating Machine (Hohsen Corporation) at 0.3 cm s^{-1} and dried at RT overnight. Hence, the electrodes were cut (9 mm diameter) and pressed at 2 tons for 2 min. While the adhesion of the slurry with PVDF is good, that of the slurry with SA is poor.

4.4. *Electrode characterization*

The electrochemical characterization of the electrodes was carried out in Swagelok cells (three-electrode mode), with Whatman GF/A separator and 500 μL of the electrolyte containing EC:DMC (1:1) 1 mol L^{-1} $LiPF_6$ (LP30, Selectilyte BASF, Germany) and, eventually, vinylene carbonate (VC, 97%, Carbolution Chemicals GmbH). Cyclic voltammetries (CVs) and galvanostatic charge/discharge (GCD) cycles at different specific current were performed at 30°C in a thermostated oven.

ACKNOWLEDGMENTS

View Article Online
DOI: 10.1039/D2MA00583B

This work was financially supported by the Estonian Research Council grant PSG312 and by the EU through the European Regional Development Fund (projects no: 2014-2020.4.01.16-0041 and 2014-2020.4.01.15-0005, TK134 EQUiTANT) as well as the European Space Agency. G.L. acknowledges the Department of Excellence program financed by the Minister of Education, University and Research (MIUR, L. 232 del 01/12/2016) for the doctoral scholarship. Prof. V. Di Noto and Dr. G. Pagot (University of Padua) are acknowledged for XPS measurements, Dr. V. Morandi and Dr. A. Migliori (CNR-IMM, Bologna) for STEM measurements and Mr. Nicolò Albanelli for XRD measurements.

Conflict of Interest

The authors declare no conflict of interest.

REFERENCES

[1] U.S. Energy Information Administration, Short-Term Energy Outlook March 2021, https://www.eia.gov/outlooks/steo/pdf/steo_full.pdf (last visit 20/03/21)

[2] J. Lau, G. Dey, S. Licht, Thermodynamic assessment of CO2 to carbon nanofiber transformation for carbon sequestration in a combined cycle gas or a coal power plant, Energy Convers. Manag. **2016**, 122, 400-410. https://doi.org/10.1016/j.enconman.2016.06.007.

[3] W. Weng, L. Tang, W. Xiao, Capture and electro-splitting of CO_2 in molten salts, J. Energy Chem. **2019**, 28, 128-143. https://doi.org/10.1016/j.jechem.2018.06.012.

[4] R. Jiang, M. Gao, X. Mao, D. Wang, Advancements and potentials of molten salt CO_2 capture and electrochemical transformation (MSCC-ET) process, Curr. Opin. Electrochem. **2019**, 17, 38-46. https://doi.org/10.1016/j.coelec.2019.04.011.

[5] A. Yu, G. Ma, J. Ren, P. Peng, F.F. Li, Sustainable Carbons and Fuels: Recent Advances of CO2 Conversion in Molten Salts, ChemSusChem. **2020**, 13, 6229-6245. https://doi.org/10.1002/cssc.202002060.

[6] J. Ge, J. Wang, J. Cheng, S. Jiao, Electrochemical Conversion of CO2 in Molten $CaCl_2$-LiCl-CaO Utilizing a Low-Cost (1-x)$CaTiO_3$-xNi Inert Anode, J. Electrochem. Soc. **2016**, 163, E230-E234. https://doi.org/10.1149/2.1361608jes.

[7] A. Douglas, R. Carter, N. Muralidharan, L. Oakes, C.L. Pint, Carbon N. Y. **2017**, 16, 572-578. https://doi.org/10.1016/j.carbon.2017.02.032.

[8] A.-L. Remmel, S. Ratso, G. Divitini, M. Danilson, V. Mikli, M. Uibu, J. Aruväli, I. Kruusenberg, Iron catalyzed growth of crystalline multi-walled carbon nanotubes from ambient carbon dioxide mediated by molten carbonates, ACS Sustain. Chem. Eng., **2021**, 10, 1, 134-145. https://doi.org/10.1021/ACSSUSCHEMENG.1C05250.

[9] J. Asenbauer, T. Eisenmann, M. Kuenzel, A. Kazzazi, Z. Chen, D. Bresser, The success story of graphite as a lithium-ion anode material – fundamentals, remaining challenges, and recent developments including silicon (oxide) composites, Sustainable Energy Fuels **2020**, 4, 5387-5416. https://doi.org/10.1039/D0SE00175A.

[10] Z. Ogumi and H. Wang, Carbon anode materials in Lithium-Ion Batteries - Science and Technologies, M. Yoshio, R. J. Brodd and A. Kozawa Eds., Springer-Verlag, New York, U.S.A., 1st edn, 2009, 49-73. https://doi.org/10.1007/978-0-387-34445-4

[11] Environmental and socio-economic challenges in battery supply chains: graphite and lithium, 2020, https://www.oeko.de/fileadmin/oekodoc/Graphite-Lithium-Env-Soc-Eco-Challenges.pdf (last visit on 20th December 2021).

[12] https://westwaterresources.net/minerals-portfolio/graphite-market/ (last visit on 7th December 2021).

[13] N.S. Hudak, Nanostructured electrode materials for lithium-ion batteries in Lithium-ion batteries: Advances and Applications, G. Pistoia Ed., Elsevier B. V., Amsterdam, The Netherlands, 2014, 57-82. http://dx.doi.org/10.1016/B978-0-444-59513-3.00004-2.

[14] I. Lahiri, W. Choi, Carbon nanostructures in lithium ion batteries: past, present, and future, Carbon Nanostructures in Lithium Ion Batteries: Past, Present, and Future, Crit. Rev. Solid State Mater. Sci. **2013**, 38, 128-166. https://doi.org/10.1080/10408436.2012.729765.

[15] S. Goriparti, E. Miele, F. De Angelis, E. Di Fabrizio, R. Proietti Zaccaria, C. Capiglia, Review on recent progress of nanostructured anode materials for Li-ion batteries, J. Power Sources **2014**, 257, 421-443. https://doi.org/10.1016/j.jpowsour.2013.11.103.

[16] P. Poizot, S. Laruelle, S. Grugeon, L. Dupont, J. Tarascon, Nano-Sized Transition-Metal Oxides as Negative-Electrode Materials for Lithium-Ion Batteries, Nature **2000**, 407, 496. DOI: 10.1038/35035045.

View Article Online
DOI: 10.1039/D2MA00583B

[17] R. Sun, Z. Qin, Z. Li, H. Fan, S. Lu, Binary zinc–cobalt metal–organic framework derived mesoporous $ZnCo_2O_4$@NC polyhedron as a high-performance lithium-ion battery anode, Dalton Trans., **2020**, 49, 14237-14242. https://doi.org/10.1039/ d0dt03132a.

[18] Y.-C. Tsai, C.-T. Kuo, S.-F. Liu, Y.-T. Lee, T.-R. Yew, Effect of Different Electrolytes on MnO_2 Anodes in Lithium-Ion Batteries, J. Phys. Chem. C **2021**, 125, 1221-1233. https://doi.org/10.1021/acs.jpcc.0c09022.

[19] H. Lai, J. Li, Z. Chen, Z. Huang, Carbon Nanohorns as a HighPerformance Carrier for MnO_2 Anode in Lithium-Ion Batteries, ACS Appl. Mater. Interfaces **2012**, 4, 2325-2328. https://doi.org/10.1021/am300378w.

[20] D.-S. Liu, D.-H. Liu, B.-H. Hou, Y.-Y. Wang, J.-Z. Guo, Q.-L. Ning, X.-L. Wu, 1D porous MnO@N-doped carbon nanotubes with improved Li storage properties as advanced anode material for lithium-ion batteries, Electrochim. Acta **2018**, 264, 292-300. https://doi.org/10.1016/j.electacta.2018.01.129.

[21] H. Zhu, Z. Li, F. Xu, Z. Qin, R. Sun, C. Wang, S. Lu, Y. Zhang, H. Fan, Ni_3Se_4@$CoSe_2$ hetero-nanocrystals encapsulated into CNT-porous carbon interpenetrating frameworks for high-performance sodium ion battery, J. Colloid Interface Sci. **2022**, 611 718–725. https://doi.org/10.1016/j.jcis.2021.11.175.

[22] X.-X. Luo, W.-H. Li, H.-J. Liang, H.-X. Zhang, K.-D. Du, X.-T. Wang, X.-F. Liu, J.-P. Zhang, X.-L. Wu, Covalent Organic Framework with Highly Accessible Carbonyls and π-Cation Effect for Advanced Potassium-Ion Batteries, Angew. Chem. Int. Ed. **2022**, 61, e202117661. https://doi.org/10.1002/anie.202117661.

[23] X. Wang, F. Sharif, X. Liu, G. Licht, M. Lefler, S. Licht, Magnetic Carbon Nanotubes: Carbide Nucleated Electrochemical Growth of Ferromagnetic CNTs from CO2, J. CO2 Util. **2020**, 40, 101218. https://doi.org/10.1016/J.JCOU.2020.101218.

[24] S. Arcaro, F.A. Berutti, A.K. Alves, C.P. Bergmann, MWCNTs produced by electrolysis of molten carbonate: Characteristics of the cathodic products grown on galvanized steel and nickel chrome electrodes, Appl. Surf. Sci. **2019**, 466, 367–374. https://doi.org/10.1016/J.APSUSC.2018.10.055.

[25] M. Demir, Z. Kahveci, B. Aksoy, N.K.R. Palapati, A. Subramanian, H.T. Cullinan, H.M. El-Kaderi, C.T. Harris, R.B. Gupta, Graphitic Biocarbon from Metal-Catalyzed Hydrothermal

View Article Online
DOI: 10.1039/D2MA00583B

Carbonization of Lignin, Ind. Eng. Chem. Res. **2015**, 54, 10731-10739. https://doi.org/10.1021/ACS.IECR.5B02614.

[26] X. Liu, X. Wang, G. Licht, S. Licht, Transformation of the greenhouse gas carbon dioxide to graphene, J. CO_2 Util. **2020**, 36, 288–294. https://doi.org/10.1016/j.jcou.2019.11.019.

[27] H. Marsh, A.P. Warburton, Catalysis of graphitisation, J. Appl. Chem. **1970**, 20, 133-142. https://doi.org/10.1002/JCTB.5010200409.

[28] I. Mochida, R. Ohtsubo, K. Takeshita, H. Marsh, Catalytic graphitization of non-graphitizable carbon by chromium and manganese oxides, Carbon N. Y. **1980**, 18, 117-123. https://doi.org/10.1016/0008-6223(80)90019-6.

[29] I. Kruusenberg, N. Alexeyeva, K. Tammeveski, J. Kozlova, L. Matisen, V. Sammelselg, et al., Effect of purification of carbon nanotubes on their electrocatalytic properties for oxygen reduction in acid solution, Carbon N. Y. **2011**, 49, 4031-4039. https://doi.org/10.1016/j.carbon.2011.05.048.

[30] R. Jiang, M. Gao, X. Mao, D. Wang, Advancements and potentials of molten salt CO_2 capture and electrochemical transformation (MSCC-ET) process, Curr. Opin. Electrochem. **2019**, 17, 38-46. https://doi.org/10.1016/j.coelec.2019.04.011.

[31] S. Ratso, P.R. Walke, V. Mikli, J. Ločs, K. Šmits, V. Vītola, et al., CO_2 turned into a nitrogen doped carbon catalyst for fuel cells and metal–air battery applications, Green Chem. **2021**, 23, 4435-4445. https://doi.org/10.1039/D1GC00659B.

[32] A. Remmel, S. Ratso, G. Divitini, M. Danilson, V. Mikli, M. Uibu, et al., Nickel and Nitrogen-Doped Bifunctional ORR and HER Electrocatalysts Derived from CO_2, ACS Sustainable Chem Eng. (accepted proofs) https://doi.org/10.1021/acssuschemeng.1c05250.

[33] H. V. Ijije, R.C. Lawrence, G. Z. Chen, Carbon electrodeposition in molten salts: Electrode reactions and applications, RSC Adv. **2014**, 4, 35808-35817. https://doi.org/10.1039/c4ra04629c.

[34] L. Hu, Y. Song, S. Jiao, Y. Liu, J. Ge, H. Jiao, et al., Direct Conversion of Greenhouse Gas CO_2 into Graphene via Molten Salts Electrolysis, ChemSusChem. **2016**, 9, 588-594. https://doi.org/10.1002/cssc.201501591.

[35] X. Wang, X. Liu, G. Licht, B. Wang, S. Licht, Exploration of Alkali Cation Variation on the Synthesis of Carbon Nanotubes by Electrolysis of CO2 in Molten Carbonates. J. CO2 Util. **2019**, 34, 303-312. https://doi.org/10.1016/j.jcou.2019.07.007.

[36] C. Julien, M. Massot, R. Baddour-Hadjean, S. Franger, S. Bach, J.P. Pereira-Ramos, Raman spectra of birnessite manganese dioxides, Solid State Ionics **2003**, 159, 345-356. https://doi.org/10.1016/S0167-2738(03)00035-3.

[37] M. Rana, V. Sai Avvaru, N. Boaretto, V. A. de la Peña O'Shea, R. Marcilla, V. Etacheri, et al., High rate hybrid MnO_2@CNT fabric anodes for Li ion batteries: properties and a lithium storage mechanism study by in situ synchrotron X-ray scattering, J. Mater. Chem. A **2019**, 7, 26596-26606. https://doi.org/10.1039/c9ta08800h.

[38] L. Eifert, R. Banerjee, Z. Jusys, R. Zeis, Characterization of Carbon Felt Electrodes for Vanadium Redox Flow Batteries: Impact of Treatment Methods, J. Electrochem. Soc. **2018**, 165, A2577-A2586. https://doi.org/10.1149/2.0531811jes.

[39] V. Di Noto, E. Negro, S. Polizzi, P. Riello, P. Atanassov, Preparation, characterization and single-cell performance of a new class of Pd-carbon nitride electrocatalysts for oxygen reduction reaction in PEMFCs, Applied Catalysis B: Environmental **2012**, 111-112, 185-199. https://doi.org/10.1016/j.apcatb.2011.09.034.

[40] H.W. Nesbitt, M. Scaini, H. Hochst, G.M. Bancroft, A.G. Schaufuss, R. Szargan, Synchrotron XPS evidence for Fe2+-S and Fe3+-S surface species on pyrite fracture-surfaces, and their 3D electronic states, American Mineralogist **2000**, 85, 850-857. https://doi.org/10.2138/am-2000-5-628.

[41] M. Oku, K. Kichinosuke, S. Ikeda, X-ray Photoelectron Spectroscopy of Manganese-Oxygen System, J. Electron. Spectros. Relat. Phenomena **1975**, 7, 465-473. https://doi.org/10.1016/0368-2048(75)85010-9.

[42] V. Di Castro, G. Polzonetti, XPS study of MnO oxidation, J. Electron. Spectros. Relat. Phenomena **1989**, 48, 117-123. https://doi.org/10.1016/0368-2048(89)80009-X.

[43] G. Elmacı, A. S. Ertürk, M. Sevim, Ö. Metin, MnO2 nanowires anchored on mesoporous graphitic carbon nitride (MnO2@mpg-C3N4) as a highly efficient electrocatalyst for the oxygen evolution reaction, Int. J. Hydrog. Energy **2019**, 44, 17995-18006. https://doi.org/10.1016/j.ijhydene.2019.05.089.

[44] Ý. A. Mørch, I. Sandvig, Ø. Olsen, I. Donati, M. Thuen, G. Skjåk-Bræk, O. Haraldseth, C. Brekken, Contrast Media and Molecular Imaging **2012**, 7, 2, 265-275. https://doi.org/10.1002/cmmi.493

View Article Online
DOI: 10.1039/D2MA00583B

[45] C. Shen, G. Hu, L.-Z. Cheong, S. Huang, J.-G. Zhang, D. Wang, Direct Observation of the Growth of Lithium Dendrites on Graphite Anodes by Operando EC-AFM, Small Methods **2018**, 2, 1700298. https://doi.org/10.1002/smtd.201700298.

[46] G. Lacarbonara, M. Rahmanipour, J. Belcari, L. Lodi, A. Zucchelli, C. Arbizzani, Electrodilatometric analysis under applied force: A powerful tool for electrode investigation, Electrochimica Acta **2021**, 375, 137938. https://doi.org/10.1016/j.electacta.2021.137938.

[47] X. Fang, X, Lu. X, Guo, Y. Mao, Y.-S. Hu, J. Wang, et al, Electrode reactions of manganese oxides for secondary lithium batteries, Electrochemistry Communications **2010**, 12, 1520-1523. doi:10.1016/j.elecom.2010.08.023.

[48] I. Kovalenko, B. Zdyrko, A. Magasinski, B. Hertzberg, Z. Milicev, R. Burtovyy, A major constituent of brown algae for use in high-capacity Li-ion batteries, Science **2011**, 334, 6052 75-79 DOI: 10.1126/science.1209150.

[49] W.-Y. Chou, Y.-C. Jin, J.-G. Duh, C.-Z. Lu, and S.-C. Liao, A facile approach to derive binder protective film on high voltage spinel cathode materials against high temperature degradation, Appl. Surf. Sci., **2015**, 355, 1272-1278. https://doi.org/10.1016/j.apsusc.2015.08.046.

[50] F. Bigoni, F. De Giorgio, F. Soavi, C. Arbizzani, Sodium Alginate: A Water-Processable Binder in High-Voltage Cathode Formulations, J. Electrochem. Soc. **2017**, 164, A6171-A6177. https://doi.org/10.1149/2.0281701jes.

[51] D.A. Shirley, High-resolution X-ray photoemission spectrum of the valence bands of gold, Phys. Rev. B, **1972**, 5, 4709-4714. https://journals.aps.org/prb/pdf/10.1103/PhysRevB.5.4709.

[52] G. Daniel, Y. Zhang, S. Lanzalaco, F. Brombin, T. Kosmala, G. Granozzi, et al., Chitosan-Derived Nitrogen-Doped Carbon Electrocatalyst for a Sustainable Upgrade of Oxygen Reduction to Hydrogen Peroxide in UV-Assisted Electro-Fenton Water Treatment, ACS Sustainable Chemistry & Engineering, **2020**, 8, 14425-14440. https://doi.org/10.1021/acssuschemeng.0c04294.